Structure-based Drug Design, Synthesis and Biological assays of *P. falciparum* Atg3-Atg8 Protein-Protein Interaction Inhibitors

Stefania Villa[a], Laura Legnani[b], Diego Colombo[c], Arianna Gelain[a], Carmen Lammi[a], Daniele Bongiorno[a], Denise P. Ilboudo[d,e], Kellen E. McGee[f], Jürgen Bosch,[f,g] Giovanni Grazioso[,a]*

[a] Dipartimento di Scienze Farmaceutiche, Università degli Studi di Milano, Via L. Mangiagalli 25, 20133 Milan, Italy.
[b] Dipartimento di Chimica, Università degli Studi di Pavia, Via Taramelli 12, 27100 Pavia, Italy.
[c] Dipartimento di Biotecnologie Mediche e Medicina Traslazionale, Università degli Studi di Milano, Via Saldini 50, 20133 Milano, Italy
[d] Dipartimento di Scienze Farmacologiche e Biomolecolari, Università degli Studi di Milano, Via Balzaretti 9, 20133 Milano, Italy
[e] Present address: Centre Universitaire Polytechnique, Université de Ouagagadougou, Fada N'Gourma, Burkina Faso
[f] Pediatric Pulmonology Division, Department of Pediatrics, Case Western Reserve University School of Medicine, Cleveland, Ohio.
[g] InterRayBio, LLC, Baltimore, Maryland.

List of authors' ORCID

Stefania Villa: 0000-0002-0636-7589
Laura Legnani: 0000-0002-3236-0364
Diego Colombo: 0000-0003-1436-2304
Arianna Gelain: 0000-0001-9104-732X
Carmen Lammi: 0000-0002-7428-4486
Daniele Bongiorno: 0000-0002-9756-2768
Denise P. Ilboudo: 0000-0002-3315-356X
Jürgen Bosch: 0000-0002-2624-4105
Giovanni Grazioso: 0000-0002-3261-9356

Abstract

The proteins involved in the autophagy (Atg) pathway have recently been considered promising targets for the development of new antimalarial drugs. In particular, inhibitors of the protein-protein interaction between Atg3 and Atg8 of *P. falciparum* retarded the blood- and liver-stages of parasite growth. In this paper, we used computational techniques to design a new class of peptidomimetics mimicking the Atg3 interaction motif, which were then synthesized by click-chemistry. Surface Plasmon Resonance (SPR) has been employed to measure the ability of these compounds to inhibit the Atg3-Atg8 reciprocal protein-protein interaction (PPI). Moreover, *P. falciparum* growth inhibition in red blood cell cultures was evaluated as well as the cyto-toxicity of the compounds.

INTRODUCTION

Malaria is one of the deadliest parasitic diseases with an estimated 212 million clinical cases in 2015, causing 429.000 deaths [1]. More than two thirds (70%) of these deaths are children under 5 years old, who are particularly susceptible to infection and illness. Malaria is thus a major killer of children in this age group, taking the life of a child every two minutes [1].

Malaria burden is caused by the *Plasmodium* parasites, transmitted through the bite of the infected female anopheline mosquitoes. The species able to infect humans are *P. falciparum*, *P. vivax*, *P. malariae*, and *P. ovale*, the first being the most lethal one. Together with *P. vivax*, *P. falciparum* accounts for more than 95% of malaria cases in the world [2]. Moreover, in South East Asia, monkey-to-human transmission of *P. knowlesi* infections have also been reported [3].

Several treatments of malaria are available, but it has become evident that all classes of drugs provoke parasite resistance, such as that recently reported for artemisinins [4,5], limiting the efficacy of the applied therapy. After intense research efforts by big pharmaceutical companies and nonprofit organizations, the new malaria vaccine *RTS,S/AS01,* developed by GlaxoSmithKline Biologicals and the "PATH Malaria Vaccine Initiative", will be rolled out in pilot projects in three countries in sub-Saharan Africa [6]. However, current available data from these studies suggest limited protection through the vaccine of about 30-40% [7]. It follows that new targets for the design and development of antimalarial drugs are urgently needed [8].

A promising strategy to develop new drugs is to target the proteases of malaria parasites, which are involved in the processes of host erythrocyte rupture, erythrocyte invasion and hemoglobin degradation. In particular, attention has been focused on falcipain-2, for which some potent inhibitors have been reported [9,10]. More recently, new experimental evidence suggested the importance of autophagy in differentiation, development and survival of pathogenic parasites [11,12] such as *P. falciparum [13]* or *Toxoplasma gondii* [14,15]. Autophagy is an intracellular degradation process in which the cellular contents are enveloped by phospholipid bilayers (autophagosome) and then fused with lysosomes or vacuoles. In mammals, over thirty different subtypes of autophagy-related proteins (Atg) are involved in this process. Among them, Atg8 seems to be essential for the formation of autophagosomal membranes. The association of Atg8 to the membrane results from its coupling with phosphatidylethanolamine (PE). This event, triggered by a post-translational modification process known as "lipidation," is accomplished by the Atg8 conjugation system. This process involves Atg proteins such as Atg4 (member of the caspase family), Atg7, Atg3 and the Atg5-Atg12 complex. The first of these (Atg4), undergoes cleavage of the *C*-terminal residues, which activates Atg8 and promotes the binding of a cysteine residue of

Atg7 to the Atg8-G116. This forms a thioester bond in an ATP-dependent manner. Then, the activated form of Atg8 is available for association with Atg3 by a thioester bond. Ultimately, the Atg5-Atg12 complex assists [16] the Atg8-Atg3 dissociation and the coupling of the Atg8' *N*-term to a PE molecule composing the membrane via an amide bond. Atg8-PE then prompts the assembly of source membranes into the membranes of autophagosomes [17].

In parasites such as *P. falciparum* [13] and *T. gondii* [15] autophagy is carried out by a simplified cellular processes, yet it is known that Atg8 was found to be essential to the parasite survival and it is expressed during all stages of their growth [18,19]. Consequently, the Atg8-Atg3 protein-protein interactions (PPIs) have been deemed a promising target for the development of new drugs active in blood and liver stages of the parasite infection [20,21].

The X-ray crystal structure of the *P. falciparum* (Pf) Atg3-Atg8 complex (PDB ID: 4EOY [13]) paved the way to the computer-aided design of new potential drug candidates, revealing that *Pf*Atg8 provides multiple sites (W and L) that anchor *Pf*Atg3 (Fig. 1). An additional region of the protein, the A-loop, has high sequence diversity among different parasites and humans. This has been the object of Hain *et al.* [20] studies leading to the identification of ALC25 (Fig. 1), which significantly inhibits the *Pf*Atg3-*Pf*Atg8 PPI, in contrast to the 4-pyridin-2-yl-1,3-thiazol-2-amine (PTA) class of compounds [21], which binds to the W- and L- sites.

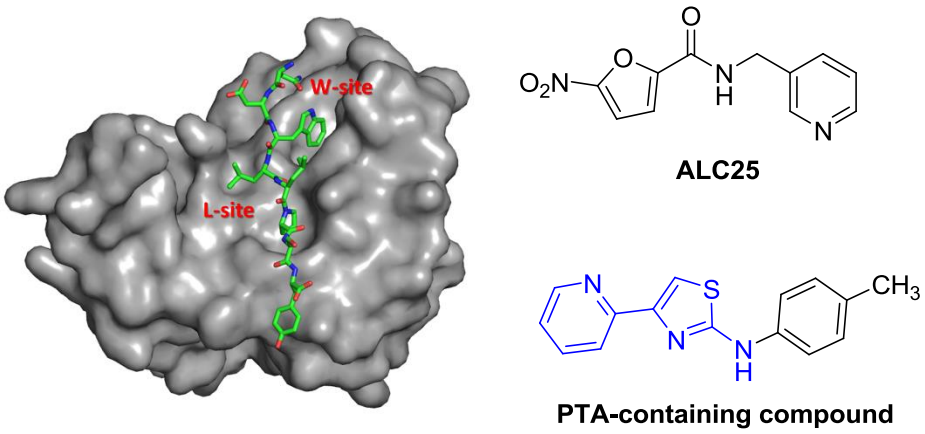

Fig. 1 X-ray structure of *Pf*Atg8 (gray surface) in complex with *Pf*Atg3 (green stick model, PDB ID: 4EOY). Chemical structures of ALC25 and of a representative PTA containing derivative, known as Atg8-Atg3 PPI inhibitors. PTA moiety is colored in blue.

In this paper, taking into account the structural insights from the *Pf*Atg3-*Pf*Atg8 X-ray complex, we report the computational design and the synthesis of new potential *Pf*Atg3-*Pf*Atg8 PPI inhibitors, and their subsequent testing by Surface Plasmon Resonance (SPR) and *P. falciparum* growth inhibition assays.

RESULTS AND DISCUSSION

Design of PPI inhibitors. PPI inhibitors are compounds capable of impairing the molecular interactions between protein partners [22]. Peptidomimetics belong to a class of PPI inhibitors that retain the molecular features of the peptide to be mimicked, in which peptide bonds are replaced by more enzymatically stable bonds. Therefore, the ideal *Pf*Atg3' peptidomimetic is a compound able to reproduce the contacts formed by the template structure (sequence NDWLLPSY), while one or more peptide bonds are replaced by new moieties. Due to the variety of interactions shaped by the amino acids of *Pf*Atg3 in the X-ray complex, the *hot spots* responsible for the PPI should be identified in order to design ligands that mimic the essential contacts only. To this aim, we identified the minimal active sequence of *Pf*Atg3 by performing molecular dynamics (MD) simulations on the solvated *Pf*Atg3/*Pf*Atg8 X-ray complex. This analysis revealed that *Pf*Atg3 interacts with *Pf*Atg8 by: i) the H-bond between the side chains of *Pf*Atg3-N103 and *Pf*Atg8-E17, ii) the projection of the *Pf*Atg3-W105 indole ring into the W-site of *Pf*Atg8 shaped by residues E17, T18, I21, P30, K58 and Y113, iii) the H-bonds of *Pf*Atg3-L106 with the backbone atoms of *Pf*Atg8-L50 and *Pf*Atg8-K58, iv) the H-bond between *Pf*Atg3-Y110 and *Pf*Atg8-Met55, v) the van der Waals (vdW) contacts between the side chain of *Pf*Atg3-L106 and those of *Pf*Atg8-F49 and *Pf*Atg8-H67, and finally vi) the vdW contacts of the *Pf*Atg3-P108' pyrrolidine ring with the *Pf*Atg8' pocket sized by residues F49, V51, F60 and M55 (L-site). MD simulations on this complex also showed that the main contributors to the *Pf*Atg8-*Pf*Atg3 PPI were located in the middle of the *Pf*Atg3 sequence (*core* region, Fig. 2A), i.e., the amino acids WLLP. In fact, after over 100 ns of MD simulations, the root mean square fluctuation (RMSF) of the Cα atoms belonging to *Pf*Atg3' *core* region was lower than 1.1 Å, at variance with the residues at the *Pf*Atg3' *C*- and *N*- terms showing higher values (Fig. 2B). This was the consequence of the stability showed by the interactions (H-bonds and vdW contacts) engaged by *Pf*Atg3-WLLP, further reinforced by the creation of two additional H-bonds between the backbone atoms of *Pf*Atg3-D104 and those of *Pf*Atg8-K47 and *Pf*Atg8-K48.

Conversely, the high conformational mobility showed by residues belonging to the *Pf*Atg3' terminal residues was caused by the loss of the H-bond between the side chains of *Pf*Atg3-N103 and *Pf*Atg8-E17. Moreover, an H-bond between *Pf*Atg3-Y110 and *Pf*Atg8-E59 was only occasionally shaped, at the expense of the *Pf*Atg3-Y110/*Pf*Atg8-Met55 contact found in the crystallized complex. All distance fluctuations over MD simulations can be found in Fig. S1, Electronic supplementary material 1.

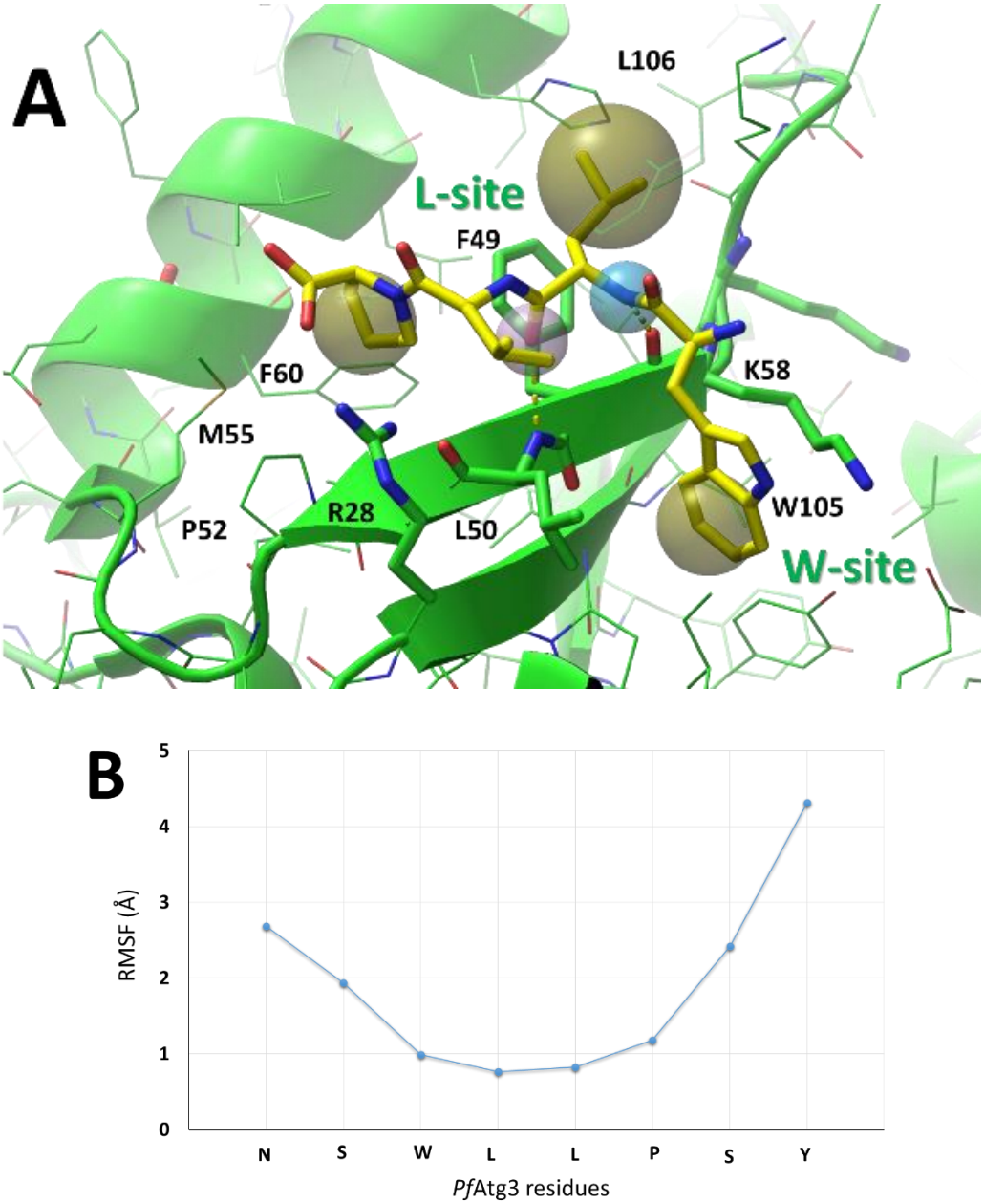

Fig. 2 A) WLLP segment of *Pf*Atg3 (yellow stick model) in complex with *Pf*Atg8 (colored as green stick model). Hydrogen bonds are represented as yellow dashed lines. **B**) Cα-RMSF of *Pf*Atg3 within the *Pf*Atg8 binding site over MD simulations.

In concordance with the calculated predictions, the WLLP sequence of *Pf*Atg3 was identified as the most suitable structure to be mimicked by new *Pf*Atg3-*Pf*Atg8 PPI inhibitors. The chemistry of peptidomimetics provides several molecular fragments capable of reproducing the peptide's primary and secondary structures [23,24]. Among them, 1,2,3-triazoles are heterocycles with interesting properties for application in peptide sciences since they are amide bioisosteres and are resistant to enzymatic degradation. These properties make 1,2,3-triazoles promising candidates for

the development of novel *Pf*Atg3 peptidomimetics with potentially improved biological profiles [23]. Furthermore, 1,4-disubstituted 1,2,3-triazoles have gained relevance in medicinal chemistry due to their synthetic accessibility by click 1,3-dipolar cycloaddition reaction between azides and alkynes under copper salts catalysis. Consequently, we designed new *Pf*Atg3 analogues in which: i) a 1,4-disubstituted 1,2,3-triazole moiety replaced the *Pf*Atg3' L106-P107 amide bond, ii) a phenyl ring replaced the isopropyl chain of *Pf*Atg3-L106, aiming to engender τ or π-π interactions with the *Pf*Atg8-F49 phenyl ring (Fig. 2A), and iii) a tryptophan was preserved in the *N*-term (Fig. 3), to optimally fill the W-site.

The substituent to be introduced in position 1 of the 1,2,3-triazole ring should occupy the *Pf*Atg8' L-site, and is expected to promote additional interactions with the *Pf*Atg8-R28 side chain surrounding that site (see Fig. 2A). In our hypothesis, a pyridine or a pyridazine ring should create suitable H-bonds with the guanidine group of *Pf*Atg8-R28; the optimal length of the spacer linking these heterocycles and the 1,2,3-triazole ring remained to be established. We therefore undertook the prediction of the size of the spacer by performing docking calculations on a small series of suitably designed peptidomimetics (Fig. 3).

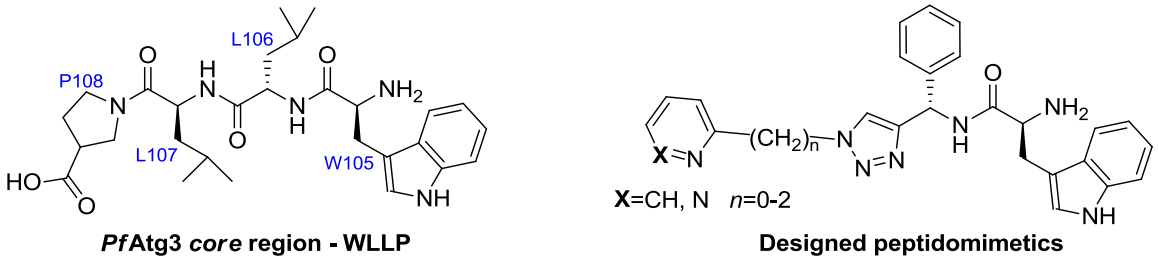

Fig. 3 General structure of the small set of designed compounds, in comparison with the template structure (*Pf*Atg3-WLLP).

The results (Fig. S2, Electronic supplementary material 1) showed that the pyridine and pyridazine derivatives, linked by an ethylene spacer to the 1,2,3-triazole ring, displayed the highest theoretical score in binding the target protein. Noteworthy, they displayed docking score identical to the one acquired by WLLP, showing experimental K_D value of 326 nM [13]. We supposed that: i) the pyridazine/pyridine ring could interact with the *Pf*Atg8-R28 side chain by hydrogen bonds, ii) the triazole ring could create a hydrogen bond with the NH of *Pf*Atg8-L50, iii) the *N*-term group (protonated) of the ligands interacted with the carbonyl group of *Pf*Atg8-K48 by a hydrogen bond, and iv) the tryptophan moiety occupied the *Pf*Atg8' W-site (Fig. 4). The superimposition of the new peptidomimetics and the *Pf*Atg3 X-ray pose showed a good overlapping between the template structure *Pf*Atg3 and the newly designed ligand structures (Fig. 4A).

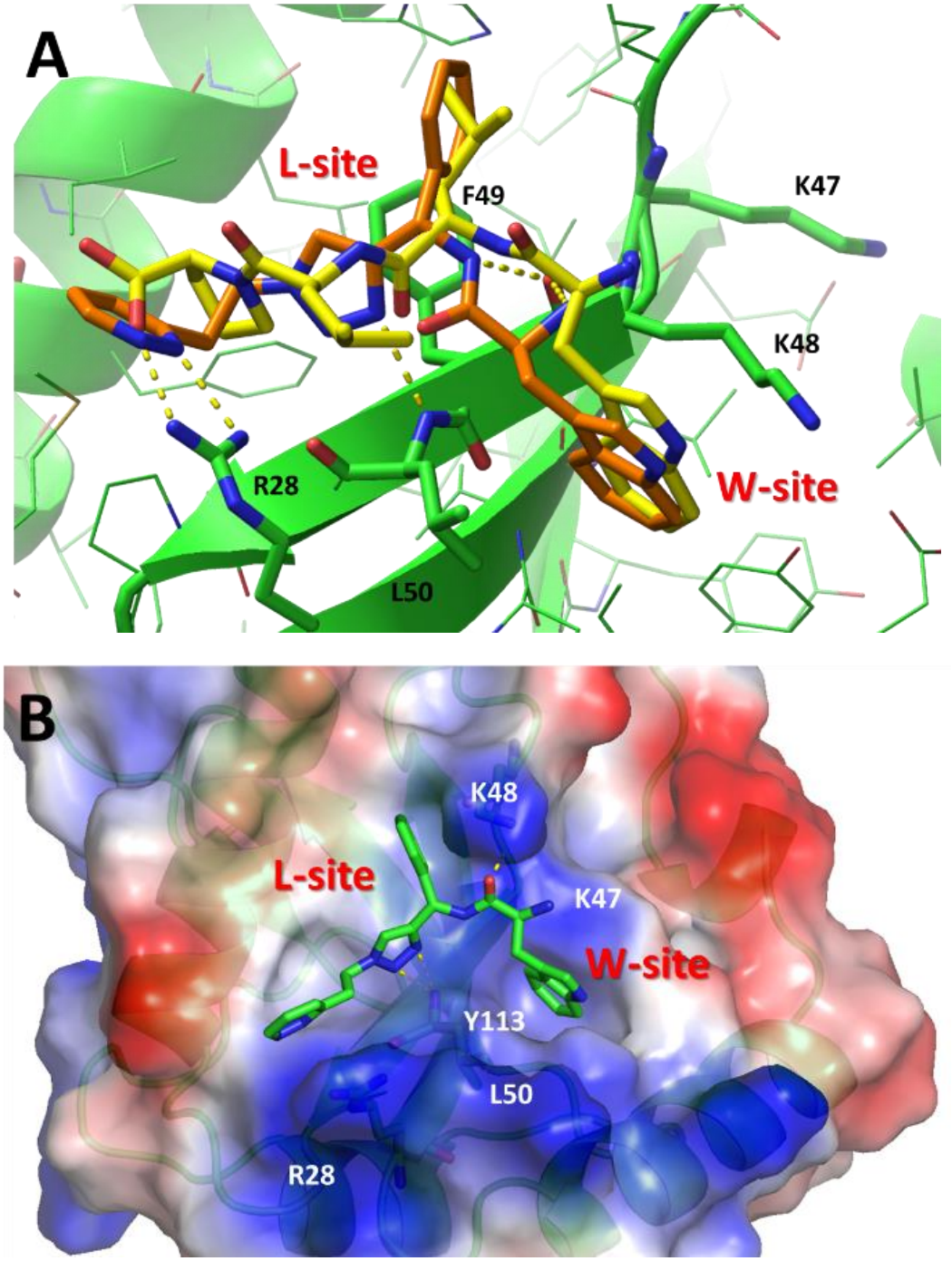

Fig. 4 A) Superimposition of pyridazine derivative (orange stick models) and *Pf*Atg3 (yellow stick models) within the binding site of *Pf*Atg8 (green stick models). Hydrogen bonds are represented as yellow dashed lines. **B)** Hypothetical binding mode of the pyridazine analogue in the *Pf*Atg8 binding site. The protein surface is colored accordingly with the partial charge of the residues, red and blue for negative and positive charges, respectively. Surface and atom partial charges were acquired by Pymol software.

MD simulations were also performed on the (*S,S*)-pyridazine analogue within *Pf*Atg8 and, at the end of the simulations (100 ns), the obtained trajectories showed that the ligand was almost stable in the binding site. In fact, the phenyl ring of the ligand created vdW contacts with the side chain of

the *Pf*Atg8-F49 (Fig. S3A, Electronic supplementary material 1). The triazole ring retained the H-bond with the NH group of *Pf*Atg8-L50 (Fig. S3B, Electronic supplementary material 1), and the indole ring was firmly inserted in the W-site (Fig. S3C, Electronic supplementary material 1). Similarly, the H-bond between the N-term of the ligand and the backbone of *Pf*Atg8-K48 was maintained (Fig. S3D, Electronic supplementary material 1). On the other hand, the pyridazine ring of the ligand was not firmly inserted in the L-site, in fact the predicted H-bond of the pyridazine ring with *Pf*Atg8-R28 during docking calculations was lost during the early stages of MD simulations (Fig. S3E, Electronic supplementary material 1).

Taking these theoretical outcomes into consideration, we synthesized the designed peptidomimetics. The planned synthetic strategy led to two pairs of diastereoisomers (Fig. 5, compounds **1**, **2** and **3**, **4**). Additional molecular modeling studies, supported by high-field NMR spectroscopy, were necessary to assign the absolute configurations to the stereocenters, after which the biological activity of the peptidomimetics was evaluated by SPR and *P. falciparum* growth inhibition tests.

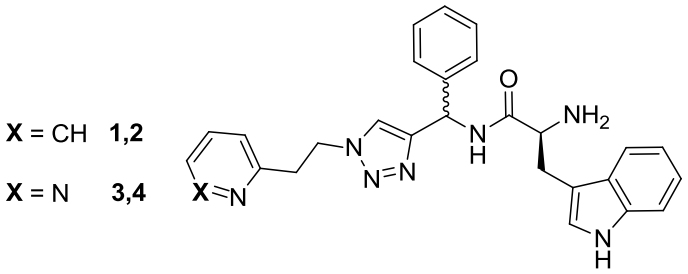

Fig. 5 Chemical structure of target compounds.

Synthesis of compounds 1-4. Synthesis of compounds **1**, **2** and **3**, **4** (Fig. 5) were performed by click reactions from alkyne **7** (Scheme 1) and the azides **12** and **13** (Scheme 2) respectively. Alkyne **7** was obtained from 1-phenyl-2-propyn-1-ol (Scheme 1) that, by treatment with acetonitrile, in presence of sulfuric acid and Na_2SO_4, was converted into the amide **5** [25]. The latter was hydrolyzed in acidic conditions and the resulting amine **6** was coupled with N-α-Boc-(L)-tryptophan, in the presence of EDAC and HOBt, to give the key intermediate **7**.

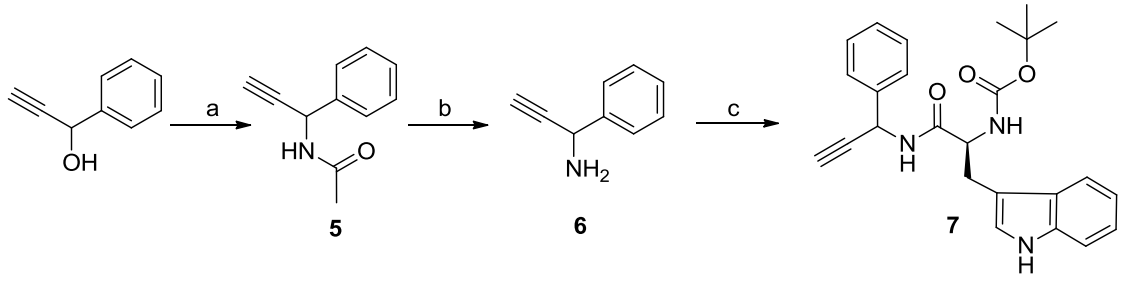

Scheme 1. Reagents and conditions: a. H_2SO_4, Na_2SO_4, CH_3CN, N_2, r.t., 48 h; b. 3.5 M HCl, 90°C, 4 h; c. N-α-Boc-(L)-tryptophan, $HOBt{\cdot}H_2O$, EDAC, CH_2Cl_2, N_2, r.t., 16 h.

Azide **12** was synthesized from the commercially available 2-(pyridin-2-yl)ethanol **8**, meanwhile azide **13** was obtained from 3-methyl pyridazine that was converted in the corresponding 2-(pyridazin-3-yl)ethanol **9** in the presence of formaldehyde (Scheme 2). The alcohols **8** and **9** were treated with methanesulfonyl chloride to afford the intermediates **10** and **11**, which were then converted into the corresponding azides **12** and **13** by treatment with NaN_3 [26].

Finally, the cycloaddition of alkyne **7** to azides **12** and **13**, in the presence of $CuSO_4$ and sodium (L)-ascorbate, provided the intermediates **14** and **15**; removal of the *tert*-butoxycarbonyl group by treatment with trifluoroacetic acid, afforded the pairs of products **1, 2** and **3, 4** respectively. The diasteroisomers were quantitatively separated by flash chromatography (Scheme 3).

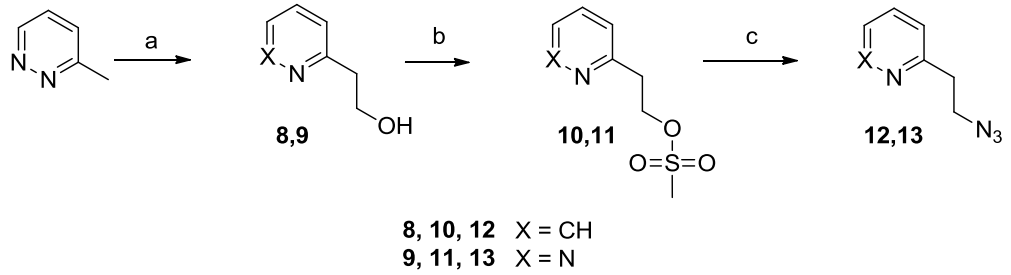

Scheme 2. Reagents and conditions: a. 37% CH_2O, piperidine, H_2O, N_2, MW, 165°C, 30 min; b. MsCl, DIPEA, CH_2Cl_2, r.t., 3 h; c. NaN_3, DMF, 70°C, 3 h.

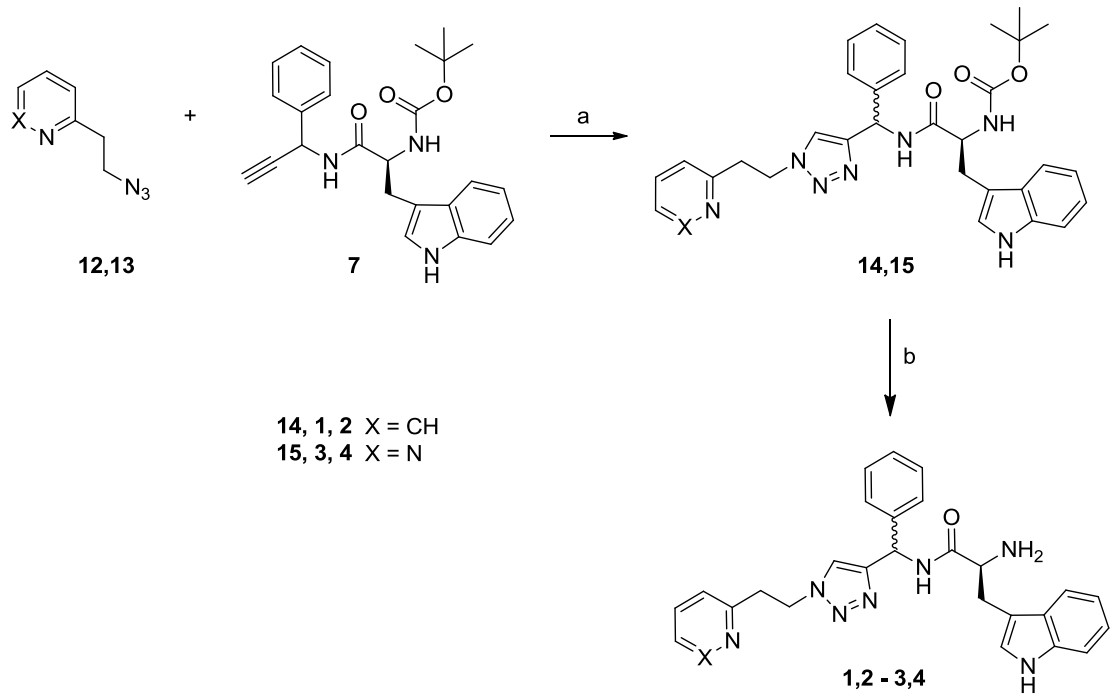

Scheme 3. Reagents and conditions: a. $CuSO_4$, sodium (L)-ascorbate, *tert*-butanol, H_2O, rt, 18 h; b. TFA, CH_2Cl_2, r.t., 3 h.

Configuration assignment of diastereoisomers 1, 2 and 3, 4. To assign the configuration of diastereoisomers **1**,**2** and **3**,**4** we decided to combine NMR spectroscopy and computational methods, as described in previous publications [27-29]. Here, the ^{1}H NMR spectra of **1** *vs* **2** and **3** *vs* **4** showed significantly different resonances of the triazole and the *ortho* phenyl protons (see Table 1), suggesting that the chemical environments of these protons is sufficiently different for the two diastereoisomers to deeply influence their chemical shifts. For this reason we decided to accomplish a complete assignment for compounds **1-4** ^{1}H resonances (Electronic Supplementary material 2) and compare the obtained data with the corresponding calculated chemical shifts based on previously optimized geometries.

The ^{1}H NMR chemical shifts of compounds **1-4** are shown in Table S1. Some NOE correlations (NOE1-4, Electronic supplementary material 2) were also related to the conformations of **1-4** and were used to drive the following modeling experiments. The conformational study was performed on the simplified structures (*R,S*)-**16** and (*S,S*)-**17** (Fig. 6) that correspond to the two epimers for compounds **1-4**. All the degrees of conformational freedom were considered; in particular, the orientation around the single bonds exemplified by the curved arrows in Fig. 6. The various geometries were all optimized at the B3LYP/6-31G(d) level [30,31].

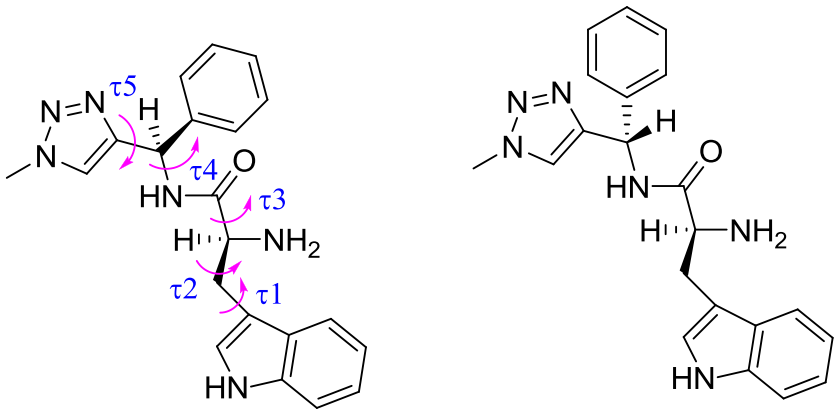

Fig. 6 Simplified structures corresponding to the epimers of compounds **1-4**.

For construction of the starting geometries, attention was initially focused on conformations showing the experimentally determined NOESY correlations (see above). Epimer **16** had a greater distribution of the population between the different conformations, while in the case of **17** only three geometries were significantly populated (Electronic supplementary material 2, Fig. S1 and

Table S2). We finally computed the ^{1}H NMR chemical shifts for each populated conformation of compounds **16** and **17** (Table 1) using GIAO NMR calculations [32,33] at the same DFT B3LYP/6-31G(d) [30,31] level already used for the optimizations. The close agreement between experimental and theoretical data of the triazole and the *ortho* phenyl protons (Table 1) allowed the configurational assignment: **1** and **3** were the diastereoisomer (*R*,*S*) while **2** and **4** were the diastereoisomer *S*,*S*.

Table 1. B3LYP/6-31G(d) GIAO calculated ^{1}H NMR chemical shift (δ, in ppm relative to TMS) of some key protons of compounds **16** and **17** based on the geometries optimized at the same level in comparison with the experimental values from the recorded spectra in compounds **1-4**.

Compound	δ *Hα*TRZ	δ *Ha*,*e*-Bn	δ *Hα*THR
16 (*R*,*S*)	6.56	7.13	6.96
17 (*S*,*S*)	7.65	6.92	6.86
1	6.85	7.09	7.07
2	7.35	6.83	6.97
3	6.97	7.13	7.09
4	7.52	6.85	7.00

Biophysical and biological investigations on compounds 1-4. We tested compounds **1-4** for *in vitro* inhibition of the plasmodial Atg8-Atg3 PPI using our established SPR competition assay [13,21,20]. Recombinant proteins for the SPR assay were purified as previously described [13]. Each inhibitor was dissolved in the running buffer and tested in triplicates in a 12-point, two-fold dilution series ranging from 0.49 µM to 1000 µM(Fig. 7A). To assess the SPR chip's integrity over the course of the experiment, the uninhibited (control) interaction of Atg8 with Atg3 in the presence of DMSO was run at regular intervals between the inhibition tests. The response of the control interaction was maintained throughout the experiment. Therefore, the chip surface was not compromised by any of the compounds, or the time it took to complete the dose-response experiment. At high concentrations (500µM – 1000µM), the compounds started precipitating in the SPR running buffer and those data were thus omitted for the IC_{50} calculation of each compound. A dose-dependent inhibition of the Atg8-Atg3 interaction was observed in all four compounds with increasing amounts of the inhibitory molecules, indicating that the described molecules are indeed able to specifically block the interaction of *Pf*Atg3 with *Pf*Atg8. The IC_{50} calculated from the normalized SPR response were **1** 20 µM, **2** 3.8 µM, **3** 12.4 µM, **4** 17.4 µM. No stereoselectivity of

the PPI inhibition was observed in the SPR assay between the (*R,S*) and the (*S,S*) diastereoisomers, however, we found stereoselectivity when we evaluated the growth inhibition of *P. falciparum* 3D7-infected blood-stage cultures using the SYBR green assay, which measures binding of a fluorescent dye to parasite-derived DNA (Fig. 7B). That the growth inhibition assays demonstrate a clear preference for the (*R,S*) diastereoisomer while the SPR assay does not is consistent with a situation in which some up-stream transporter or process, present only in *in culture* context, is stereoselective even though the PPI inhibition itself is not. This may be observed in the result that, as measured by SPR, compound **2** had the most prominent inhibition with an IC_{50} of 3.8 µM, yet was found to be essentially inactive in the *in culture* SYBR green assay with an IC_{50} of about 560 µM. *In culture,* compound **1** had the most prominent, albeit still modest, inhibitory effect with an IC_{50} of about 40 µM. In support of stereoselectivity of the inhibitory effect in an *in culture* context, an approximately ten-fold increase in potency was observed both times the (*R,S*) diastereoisomer was used to prevent *P. falciparum* growth, implying the *in culture* processes are more efficient at transporting the (*R,S*) diastereoisomer into the cell and thereby providing compound **1** with access to the *Pf*Atg3 and *Pf*Atg8 interface. The counterintuitive result of **2** emphasizes the need for the cross-validation of assays using multiple readout methods, enabling the early differentiation of putative lead compounds.

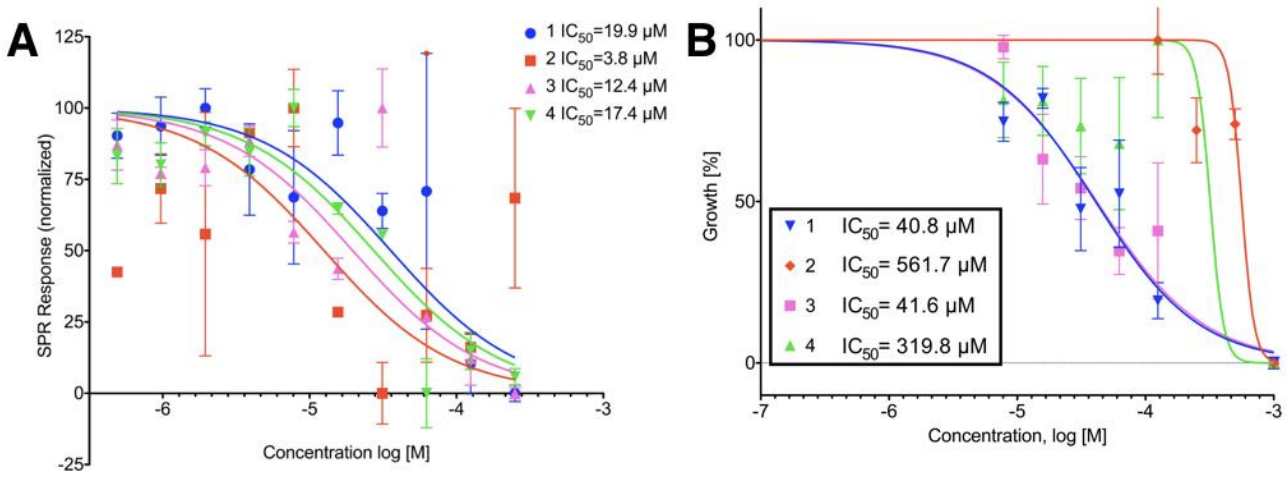

Fig. 7 A) SPR PPI inhibition study. The normalized SPR response for each compound is plotted versus the logarithmic inhibitory concentration in M. All four compounds were tested in the range of 0.4 – 250 µM. **B)** SYBR green growth inhibition assay of *P. falciparum* 3D7 strain with calculated IC_{50} values. Compound **1** and **3** are the *R,S* diastereoisomers while **2** and **4** are the *S,S* diastereoisomers.

Compounds 1 and 2 do not show any cytotoxic effect on HepG2 viability. MTT experiments were performed in order to exclude the potential toxic effects of compounds **1** and **2** on the HepG2 cell line (Fig. 8). Compounds **1** and **2** were tested at concentrations ranging from 1 to 100 µM and

no significant cell mortality was observed at all tested doses after 24 and 48 h treatment *versus* vehicle (C, DMSO). These data suggest that both compounds do not induce any cell mortality in this dose range.

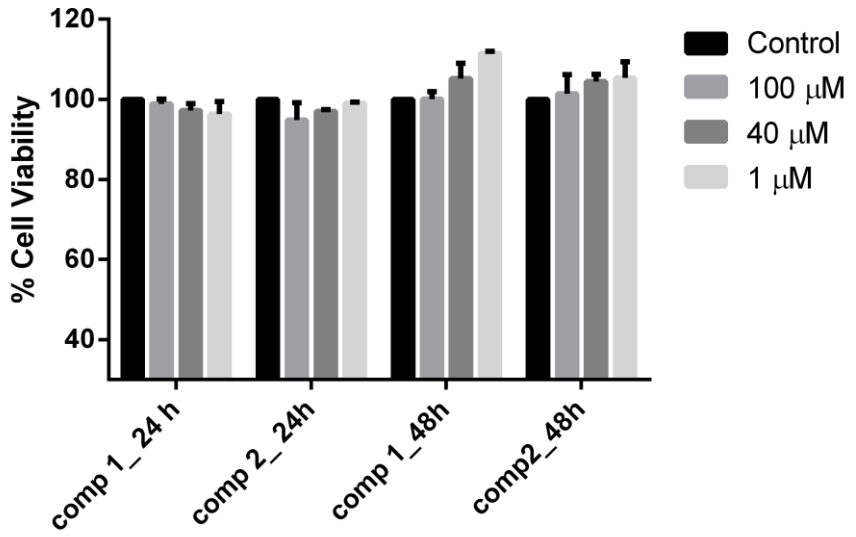

Fig. 8 . Bar graphs indicating the results of MTT cell viability assay of HepG2 cells after compounds **1** and **2** treatment for 24 and 48 h. The data points represent the averages ± SD of three independent experiments in triplicate.

CONCLUSION

The crystal structure of the *Pf*Atg3-*Pf*Atg8 complex ushered in the possibility of computer-aided drug design of new *Pf*Atg3' peptidomimetics with potential antimalarial activity. In this paper, the X-ray crystal structure of the *Pf*Atg3-*Pf*Atg8 complex was geometrically optimized by energy minimization and MD simulations. The analysis of the resulting trajectories supported the evidence that the WLLP sequence of *Pf*Atg3 displayed the lowest conformational freedom in the *Pf*Atg3-*Pf*Atg8 complex; therefore WLLP was chosen as template for the design of new peptidomimetics incorporating a substituted 1,2,3-triazole ring, which is a known amide bioisostere. A small set of compounds was designed and screened by docking calculations, and two pairs of diastereoisomers (compounds **1-4**) were then selected and synthesized through a click-chemistry approach. In each diastereomeric pair, NMR and conformational analysis studies allowed unequivocal assignment of the absolute configuration to the stereocentres.

Biological assays showed that the *Pf*Atg3-*Pf*Atg8 association was inhibited in the SPR assay by both diastereoisomers. Noteworthy, the (*R,S*) diastereoisomers **1** and **3** were about tenfold more potent in inhibiting parasite growth than their corresponding (*S,S*) counterparts **2** and **4**. This suggests that inhibitors with the (*R,S*) configuration of the peptidomimetic drug could be either more efficiently transported across the red blood cell membrane and/or the parasite plasma

membrane, or that inhibitors having the (*S,S)* configuration are degraded faster in a cellular context by peptidases.

The most active isomers **1** and **3** showed a comparable IC_{50} value of about 40 μM in a *Plasmodium falciparum* growth inhibition assay. MTT experiments on compounds **1** and **2** showed that they do not induce any cell mortality. However, further efforts are needed to design more active compounds, capable to fully and stably occupy the L-site of the target protein *Pf*Atg8. In fact, as suggested by MD simulations, the pyridazine moiety of the pyridazine derivatives (**3**-**4**) could not be firmly bound in the L-site of *Pf*Atg8, and this could explain the low biological activity showed by these compounds.

The results attained in this initial study point at the research of peptidomimetics in this area to novel inhibitors endowed with the (*R,S*) absolute configuration, with the pyridazine moiety that should conceivably be replaced by a molecular fragment more stably bound to the *Pf*Atg8' L-site. Computational and synthetic studies aiming to identify more efficient *Pf*Atg3-*Pf*Atg8 PPI inhibitors are still ongoing.

EXPERIMENTAL PROTOCOL

Molecular dynamics simulations. MD simulations of the *Pf*Atg3-*Pf*Atg8 and the *Pf*Atg8/**4** complexes were performed by assigning the force field parameters of AMBER12 [34] package. Accordingly, the proteins were treated by the *ff12SB* force fields, and GAFF was employed for the treatment of ligand [35], and the TIP3P model [36] was used to represent the solvent molecules. A cubic box of water, with a minimum distance of 20 Å from the protein surface, was built. Prior to starting MD simulations, a minimization of the bulk water molecules was carried out, using a gradient criterion convergence of 0.2 kcal mol-1 Å-1. Then, the whole system was optimized by applying a convergence criterion of 0.0001 kcal mol-1 Å-1 and next equilibrated gradually increasing the temperature to 300 K, over 60 ps. Finally, a production run of 100 ns was performed. Van der Waals and short-range electrostatic interactions were taken into account within a 10 Å cutoff, while long-range electrostatic interactions were assessed using particle mesh Ewald method [37]. Berendsen's coupling algorithms [38] were active to maintain the temperature at 300 K and the pressure of the system at 1 atm, by a coupling constant set to 1.5 ps. *Pmemd.cuda* module of AMBER12 performed the production runs of MD simulations.

Docking studies. Docking calculations of the (*S,S*) pyridazine analogue (Fig. 5) were performed by GOLD5.2.2 algorithm [39] using the crystal structure of *Pf*Atg8 deposited in the Protein Data

Bank with the code 4EOY, chain B [13]. The binding site was defined by selecting the residues included in a sphere with a radius of 13.0 Å from the Cα atom of Phe49. Amino and carboxyl groups were considered in the ionized form for consistency with the expected protonation state at physiological pH. ChemPLP scoring function [40] was employed while the genetic algorithm parameters were kept at their default values, as already done in previous studies [41]. At the end of docking calculations, poses were clustered by the complete-linkage method [39]. This is an agglomerative hierarchical clustering algorithm in which, initially, each element is located in a different singleton cluster, then clusters are combined into larger clusters until all elements are in the same cluster. At each step, the two clusters separated by the shortest distance are combined [39]. Finally, the clusters were ranked depending on the obtained score. The solution representative of each cluster was the one which obtained the highest docking score.

Chemistry. Reagents and solvents were purchased from Sigma-Aldrich and used without further purification. Reactions were performed through conventional conditions or by a microwave synthesizer (Initiator 2.0 Biotage). The reactions involving air-sensitive reagents were carried out under nitrogen atmosphere and anhydrous solvents were used when necessary. Reactions were monitored by thin layer chromatography analysis on aluminum-backed Silica Gel 60 plates (70-230 mesh, Merck), using an ultraviolet fluorescent lamp at 254 nm and 365 nm. Visualization was aided by opportune staining reagents. Purification of intermediates and final compounds was performed by flash chromatography using Geduran® Si 60 (40-63 µm, Merck).

^{1}H and ^{13}C NMR spectra were recorded in $CDCl_3$ and CD_3OD on a Variant 300 MHz Oxford equipped with a non-reverse probe at 25° C. Chemical shifts are expressed as δ (ppm) and are referenced to residual solvent proton/carbon peak. Multiplicity is reported as *s* (singlet), *br s* (broad singlet), *d* (double), *t* (triplet), *q* (quartet), *m* (multiplet), *dd* (double of doublets), *dt* (doublet of triplets). The coupling constants (J-values) are given in Hertz (Hz). All spectroscopic data match the assigned structures. ESI-MS analyses were performed by using a LQT- Orbitrap XL mass spectrometer (Thermo Fisher Scientific) with an electrospray ionization source (Finningan IonMax). Melting points were determined on a Buchi Melting Point B540 instrument. Optical rotations were determined by the polarimeter JASCO P-1010, at 25 °C.

*Procedure for the synthesis of tert-butyl ((2S)-3-(1H-indol-3-yl)-1-oxo-1-((1-phenylprop-2-yn-1-yl)amino)propan-2-yl)carbamate (**7**). Synthesis of N-(1-phenylprop-2-yn-1-yl)acetamide (**5**)* [25]. To a suspension of 1-phenyl-2-propyn-1-ol (500 mg, 3.783 mmol) and Na_2SO_4 (537 mg, 3.783

mmol) in CH_3CN (6 mL) at -25°C under stirring, a solution of 97% H_2SO_4 (1 mL) in CH_3CN (3.9 mL) was added dropwise. The mixture was stirred at room temperature for 48 h. Afterwards the solvent was concentrated and ice was added to the suspension that was extracted by diethyl ether (3 × 5 mL) and dichloromethane (3 × 5 mL). The organic layer was dried and evaporated under vacuum. The crude was purified by flash chromatography (eluent mixture: diethyl ether/petroleum ether 5:5) to give the white solid **5** (655 mg, 3.782 mmol).

Yield: quantitative; M.p. 88.8-89.8 °C; ^{1}H NMR (300 MHz, $CDCl_3$) δ 1.62 (s, 1H), 2.02 (s, 3H), 2.49 (d, *J* = 3 Hz, 1H), 6.02 (d, *J* = 3 Hz), 7.23-7.55 (m, 5H).

*Synthesis of 1-phenylprop-2-yn-1-amine (**6**)* [42]. N-(1-phenylprop-2-yn-1-yl)acetamide (**5**) (465 mg, 2.684 mmol) was suspended in 3.5M HCl (15.5 mL) and heated to 90°C under stirring for 5 h. After cooling, the solution was extracted with diethyl ether (1 × 5 mL) and the aqueous layer was basified by adding solid $NaHCO_3$ until pH 8.5 and subsequently extracted with diethyl ether (3 × 10 mL). The organic layer was dried and concentrated *in vacuo*. The crude was purified by flash chromatography (eluent mixture: diethyl ether/ petroleum ether, 5:5) to obtain amine **6** as purple oil (242 mg, 1.845 mmol).

Yield: 69%; ^{1}H NMR (300 MHz, $CDCl_3$) δ 2.057 (s, 2H), 2.49 (d, *J* = 3 Hz, 1H), 4.79 (d, *J* = 3 Hz, 1H), 7.23-7.58 (m, 5H).

Synthesis of *tert-butyl ((2S)-3-(1H-indol-3-yl)-1-oxo-1-((1-phenylprop-2-yn-1-yl)amino)propan-2-yl)carbamate* (**7**). A solution of N-α-Boc-(L)-tryptophan (235 mg, 0.772 mmol) dissolved anhydrous dichloromethane (30 mL) under nitrogen atmosphere was cooled by an ice bath, and 1-phenylprop-2-yn-1-amine (**6**) (160 mg, 1.220 mmol) was added. When the mixture reached the room temperature, monohydrated HOBt (178 mg, 1.165 mmol) and EDAC (231 mg, 1.206 mmol) were added. The mixture was stirred at room temperature for 16 h and then the solvent was evaporated under reduced pressure. The crude was purified by flash chromatography (eluent mixture: ethyl acetate/petroleum ether 3:7) to afford a yellow oil **7** (305 mg, 0.731 mmol) as diastereoisomeric mixture.

Yield: 95%; ^{1}H NMR (300 MHz, $CDCl_3$) δ 1.41 (s, 9H), 1.72 (br s, 1H), 2.40 (s, 1H), 3.14-3.23 (m, 1H), 3.27-3.37 (m, 1H), 4.45 (br s, 1H), 6.29 (dd, *J* = 9, 24 Hz, 1H), 7.11-7.37 (m, 10H), 7.67 (d, *J* = 9 Hz, 1H), 7.99 (d, *J* = 24 Hz, 1H); ^{13}C NMR (75 MHz, $CDCl_3$) δ 28.01 (*C*H_2, THR β), 28.20 (3*C*H_3), 44.40 and 44.44 (diast. *C*H, Bn), 54.22 (*C*H, THR α), 73.04 (≡*C*H), 81.26 (≡*C*− or

C−O), 81.29 (*C*−O or ≡*C*−), 110.10 (*C*, THR h), 111.21 (*C*H, THR b), 118.70 and 118.76 (diast. *C*H, THR e), 119.75 (*C*H, THR d), 122.18 (*C*H, THR c); 123.34 and 123.41 (diast. *C*H, THR a), 126.86 and 126.89 (diast. 2*C*H, Bn a, e), 127.29 (*C*, THR g), 128.08 (*C*H, Bn c), 128.56 and 128.59 (diast. 2*C*H, Bn b, d), 136.15 and 136.21 (diast. *C*, Bn f), 137.71 (*C*, THR f or C=O Boc), 137.79 (THR f or C=O Boc), 170.77 (C=O). Chemical Formula: $C_{25}H_{27}N_3O_3$. Molar mass: 417.51 g/mol; MS (ESI) *m/z* 440.2 $[M+Na]^+$.

*Procedure for the synthesis of 2-(pyridazin-3-yl) ethanol (**9**).* To 3-methylpyridazine (500 mg, 5.313 mmol) in a microwave vessel under nitrogen atmosphere, 37% formaldehyde (730 mg, 7.975 mmol), water (1 mL) and piperidine (0.20 mL) were added. The reaction mixture was heated at 165°C for 30 min in a microwave synthesizer (300 Watts). The solvent was then evaporated under reduced pressure and the crude was purified by flash chromatography (eluent mixture: dichloromethane/methanol, 9:1) to give the alcohol **9** (259 mg, 2.086 mmol) as a yellow oil.

Yield: 40%; ^{1}H NMR (300 MHz, $CDCl_3$) δ 2.99 (br s, 1H), 3.19 (t, *J* = 6 Hz, 2H), 4.11 (t, *J* = 6 Hz, 2H), 7.37-7.46 (m, 2H), 9.03-9.07 (m, 1H).

*General procedure for the syntheses of 2-(pyridin-2-yl)ethyl methanesulfonate (**10**) and 2-(pyridazin-3-yl)ethyl methanesulfonate (**11**).* To the opportune alcohol (2 mmol) in dichloromethane (5 mL), DIPEA (4 mmol) was added and the solution was cooled at 0°C. Subsequently methanesulfonyl chloride (2.2 mmol) was added and the mixture was stirred at room temperature for 3 h. Afterwards water (5 mL) was added and the organic layer was separated, washed with a solution of $NaHCO_3$ (5 mL), dried and concentrated under vacuum.

The obtained yellow oils were used in the next step without further purification.

Intermediate **10**. Yield: quantitative; ^{1}H NMR (300 MHz, $CDCl_3$) δ 2.95 (s, 3H), 3.42 (t, *J* = 6 Hz, 2H), 4.75 (t, *J* = 6 Hz, 2H), 7.39-7.48 (m, 2H), 9.08-9.14 (m, 1H);

Intermediate **11.** Yield: 79%; ^{1}H NMR (300 MHz, $CDCl_3$) δ 2.87 (s, 3H), 3.20 (t, *J* = 6.3 Hz, 2H), 4.64 (t, *J* = 6.3 Hz, 2H), 7.12-7.23 (m, 2H), 7.58-7.66 (m, 1H) 9.08-9.14 (m, 1H).

*General procedure for the syntheses of 2-(2-azidoethyl)pyridine (**12**) and 3-(2-azidoethyl)pyridazine (**13**).* To a solution of the suitable mesylate (1.3 mmol) in DMF (3 mL) under stirring, NaN_3 (4 mmol) was added and the mixture was heated at 70°C for 3 h, then the solvent was evaporated under reduced pressure. The crudes were purified by flash chromatography (eluent mixture: dichloromethane/methanol 95:5) to give the azides as yellow oils.

Intermediate **12**. Yield: 63% (from intermediate **10**); ^{1}H NMR (300 MHz, $CDCl_3$) δ 3.23 (t, *J* = 6.6 Hz, 2H), 3.83 (t, *J* = 6.6 Hz, 2H), 7.39-7.48 (m, 2H), 9.08-9.14 (m, 1H);

Intermediate **13**. Yield: 57% (from intermediate **11**); ^{1}H NMR (300 MHz, $CDCl_3$) δ 3.06 (t, *J* = 6.9 Hz, 2H), 3.71 (t, *J* = 6.9 Hz, 2H), 7.13-7.22 (m, 2H), 7.58-7.66 (m, 1H), 9.52-9.58 (m, 1H);

*General procedure for the syntheses of tert-butyl ((2S)-3-(1H-indol-3-yl)-1-oxo-1-((phenyl(1-(2-(pyridin-2-yl)ethyl)-1H-1,2,3-triazol-4-yl)methyl)amino)propan-2-yl)carbamate (**14**) and tert-butyl ((2S)-3-(1H-indol-3-yl)-1-oxo-1-((phenyl(1-(2-(pyridazin-3-yl)ethyl)-1H-1,2,3-triazol-4-yl)methyl)amino)propan-2-yl)carbamate (**15**).* To the solution of the alkyne **7** (0.5 mmol) and the opportune azide (0.5 mmol) dissolved in *tert*-butanol (120 mL), $CuSO_4$ (0.8 mmol), sodium (L)-ascorbate (2 mmol) and water (60 mL) were respectively added. After stirring at room temperature for 18 h, the mixture was extracted with dichloromethane (3 × 40 mL) and washed with brine (1 × 20 mL). The organic layer was dried and concentrated to reduced pressure. The crudes were purified by flash chromatography (eluent mixture: dichloromethane/methanol 95:5) obtaining the required triazoles as yellow oils.

Intermediate **14**. Yield: 61%; ^{1}H NMR (300 MHz, CD_3OD) δ 1.09-1.25 (m, 1H), 1.38 (s, 9H), 3.01-3.12 (m, 1H), 3.14-3.23 (m, 1H), 3.28-3.32 (m, 2H), 3.51 (t, *J* = 6.6 Hz, 2H), 4.40 (t, *J* = 7.2 Hz, 1H), 6.13 (d, *J* = 7.2 Hz, 1H), 6.82-7.63 (m, 15H), 9.00 (s, 1H).

Intermediate **15.** Yield: 92%; ^{1}H NMR (300 MHz, $CDCl_3$) δ 1.39-1.45 (m, 10H), 3.11-3.22 (m, 1H), 3.27-3.40 (m, 3H), 4.53 (br s, 1H), 4.64-4.74 (m, 2H), 6.09-6.21 (m, 1H), 6.56-7.36 (m, 14H), 7.53-7.70 (m, 2H), 8.51-8.59 (m, 1H).

*General procedure for the syntheses of (2S)-2-amino-3-(1H-indol-3-yl)-N-(phenyl(1-(2-(pyridin-2-yl)ethyl)-1H-1,2,3-triazol-4-yl)methyl)propanamides (**1,2**) and (2S)-2-amino-3-(1H-indol-3-yl)-N-(phenyl(1-(2-(pyridazin-3-yl)ethyl)-1H-1,2,3-triazol-4-yl)methyl)propanamides (**3,4**).* To the solution of the opportune Boc-derivative (0.3 mmol) in dichloromethane (3 mL) trifluoroacetic acid (3 mL) was slowly added dropwise under stirring, at room temperature. After 3 h, the solution was treated with aqueous $NaHCO_3$ until pH 8.5 and the organic layer was dried and concentrated under

vacuum. The crudes were purified by flash chromatography (eluent mixture: dichloromethane/methanol 9:1) affording the expected products.

Product **1**. Chemical Formula: $C_{26}H_{26}N_8O$. Molar mass: 466.55 g/mol. Yield: 44%; light yellow solid; M.p. 230°C dec.; MS (ESI) *m/z* 489.4 $[M+Na]^+$. $[\alpha]_D^{25}$ = +16.2 (c = 0.4 M, CH_3OH). ^1H and ^{13}C NMR spectra data are reported in Table S1 in Electronic supplementary materials 2

Product **2**. Chemical Formula: $C_{26}H_{26}N_8O$. Molar mass: 466.55 g/mol. Yield: 39%; light yellow solid; M.p. 182.4°C; MS (ESI) *m/z* 489.4 $[M+Na]^+$. $[\alpha]_D^{25}$ = +9.3 (c = 0.4 M, CH_3OH). ^1H and ^{13}C NMR spectra data are reported in Table S1 in Electronic supplementary materials 2.

Product **3**. Chemical Formula: $C_{27}H_{27}N_7O$. Molar mass: 465.56 g/mol. Yield: 32%; light pink foam; MS (ESI) *m/z* 466.2 $[M+1]^+$. $[\alpha]_D^{25}$ = +7.4 (c = 0.8 M, CH_3OH).^1H and ^{13}C NMR spectra data are reported in Table S1 in Electronic supplementary materials 2.

Product **4**.Chemical Formula: $C_{27}H_{27}N_7O$. Molar mass: 465.56 g/mol. Yield: 50%; light yellow foam; MS (ESI) *m/z* 466.2 $[M+1]^+$. $[\alpha]_D^{25}$ = +13.02 (c = 0.8 M, CH_3OH). ^1H and ^{13}C NMR spectra data are reported in Table S1in Electronic supplementary materials 2.

NMR Spectroscopy. NMR spectra of compounds **1-4** and **7** were recorded with a Bruker AVANCE-500 spectrometer operating at 500.13 MHz for ^1H or at 125.76 MHz for ^{13}C NMR spectra using a 5 mm z-PFG (pulsed field gradient) broadband reverse probe. Chemical shifts are reported on the δ (ppm) scale and are relative to residual CH_3OD at 3.30 ppm (central line) for ^1H NMR spectra, and relative to CD_3OD at 47.0 ppm (central line) for ^{13}C NMR spectra. The data were collected and processed by XWIN-NMR software (Bruker) running on a PC with Microsoft Windows xp. Compounds (about 15 mg) were dissolved in CD_3OD (0.75 mL). The solutions were put in a 5 mm NMR tube and the spectra recorded at 296 K. The signal assignment was given by a combination of 1D and 2D (COSY, NOESY and HSQC) experiments, using standard Bruker pulse programs. The ^1H-^1H and ^{13}C-^1H bond correlations were confirmed by COSY and HSQC experiment using Z-PFGs. The pulse widths were 7.50 μs (90°) for ^1H and 14.75 μs (90°) for ^{13}C. Typically 32 K data points were collected for one-dimensional spectra. Spectral width was 14.0 ppm (7002 Hz) for ^1H NMR (digital resolution: 0.21 Hz per point).

2D experiments parameters were as follows. For ^{1}H-^{1}H correlations: relaxation delay 2.0 s, data matrix 1 K × 1 K (512 experiments to 1 K zero filling in F_1, 1 K in F_2), 2 or 32 transients in each experiment for COSY and NOESY respectively, spectral width 9.00 ppm (4496.4 Hz). The NOESY spectra were generated with a mixing time of 1.0 s and acquired in the TPPI mode. There were not significant differences in the results obtained at different mixing times (2.0 – 3.0 s). For ^{13}C-^{1}H correlations (HSQC): relaxation delay 2.5 s, data matrix 1K × 1K (512 experiments to 1 K zero filling in F_1, 1K in F_2), 6 transients in each experiment, spectral width 7.0 ppm (3501 Hz) in the proton domain and 180.0 ppm (22638 Hz) in the carbon domain. A sinebell weighting was applied to each dimension. All 2D spectra were processed with the Bruker software package.

Conformational analysis. All the calculations were carried out using the GAUSSIAN09 program package [43]. Optimizations were performed at the B3LYP/6-31G(d) level [30,31], considering all degrees of conformational freedom and on the basis of experimental NOESY correlations. Vibrational frequencies were computed at the same level of theory to verify that the optimized structures were minima. The population percentages were calculated through the Boltzmann equation. GIAO NMR calculations were carried out at the B3LYP/6-31G(d) level [30,31].

Surface Plasmon Resonance Assays. SPR runs were conducted on a Biacore T100 instrument (GE Healthcare) at 25°C with a flow rate of 50 μL/min, unless otherwise specified. Running buffer (RB) consisted of 1x PBS (1 mM KH_2PO_4, 5.6 mM Na_2HPO_4, 154.5 mM NaCl, pH 7.4), 0.01% v/v P20, and varying amounts of DMSO (Quality Biologicals). Binding and equilibrium constants were determined with Scrubber (BioLogic™). A double-referencing method was applied to correct for nonspecific binding to the chip with interspersed blank injections correcting for baseline drifts. Changes in refractive index due to DMSO were accounted for with a DMSO calibration curve. Furthermore, a positive control experiment using a defined amount of the binding partner of Atg8 in the presence of DMSO was interspersed every 4th injection. Using this positive control allows monitoring the decay of the ligand attached to the SPR chip. No decay was observed throughout the experiments,

P. falciparum **Blood Stage Culturing**. Cultures of *P. falciparum* 3D7 strain were maintained using modified, previously published methods at 37°C, 2% hematocrit of human red blood cells [44]. Complete culture media consisted of sterile RPMI 1640 media (Life Technologies)

supplemented with 10% human serum and 0.005% hypoxanthine and buffered with final concentrations of 0.6% HEPES and 0.26% $NaHCO_3$. The *P. falciparum* 3D7 strain was maintained at 5% CO_2, 5% O_2, and 90% N_2 atmosphere.

SYBR Green I Growth Inhibition Assay. Ten microliters of 10x compound diluted in RPMI 1640 media (Gibco) with a constant concentration of 1% DMSO were added to a 96 well plate (Costar), 90 µL of 1.5% ring stage, synchronized with 5% w/v sorbitol *P. falciparum* 3D7 parasites, 1% hematocrit, in culture media with 10% v/v human serum with 10 µg/mL gentamycin. Each compound concentration and 1% v/v DMSO controls were run in triplicate. Plates were incubated at 37°C in 5% O_2, 5% CO_2, and 90% N_2 for 72 h. Plates were frozen, thawed, and incubated with 100 µL 2× SYBR green in lysis buffer (20 mM Tris pH 7.5, 5 mM EDTA, 0.008% Saponin, 0.08% TritonX-100) in the dark for at least 1 h. Fluorescence was measured with a plate reader (SpectraMax I3X, Molecular Dimensions) at excitation/emission wavelengths of 485/ 535 nm. Analysis was carried out using GraphPad Prism and treating the DMSO vehicle control as 100% growth and the 100 µM Chloroquine control as 0% growth. Automatic outlier control was employed using log (inhibitor) *versus* the normalized response.

MTT assay. The HepG2 cell line was bought from ATCC (HB-8065, ATCC from LGC Standards, Milan, Italy) and was cultured in DMEM high glucose with stable L-glutamine, supplemented with 10% FBS, 100 U/mL penicillin, 100 µg/mL streptomycin (complete growth medium) with incubation at 37 °C under 5% CO_2 atmosphere. HepG2 cells were used for no more than 20 passages after thawing, because the increase in number of passages may change the cell characteristics and impair assay results. A total of 3 x 10^4 HepG2 cells/well were seeded in 96-well plates and treated with 100.0 40.0 and 1.0 µM of compounds 1 and 2, respectively, or vehicle (DMSO) in complete growth media for 24 and 48 h. Subsequently, the treatment solvent was aspirated and 100 µL/well of MTT filtered solution added for 2 h. After the incubation time, 0.5 mg/mL MTT solution was aspirated and 100 µL/well of MTT lysis buffer (8 mM HCl + 0.5% NP-40 in DMSO) added. After 5 min of slow shaking, the absorbance at 570 nm and 630 nm (reference wavelength) were read by a microplate reader Synergy H1 from BioTek Germany (Bad Friedrichshall, Germany).

Electronic supplementary material

"Supplementary_material1.pdf" contains the atoms distance fluctuation plots acquired by MD simulations, and a figure showing the docking results. Conformational analysis, NMR studies and spectra can be found in Supplementary_material2.pdf.

Author information

Corresponding Author. Giovanni Grazioso, Email: *giovanni.grazioso@unimi.it*

Author Contributions. The manuscript was written through contributions of all authors. All authors have given approval to the final version of the manuscript.

Notes

The authors declare no competing financial interests.

Funding sources

We acknowledge the CINECA and the Regione Lombardia award under the LISA initiative, for the availability of high performance computing resources and support. We thank the Johns Hopkins Malaria Research Institute parasite and insectary facility for assistance with our experiments. This work was partially funded through The Bloomberg Family Foundation (J.B.). We thank Professors D. Taramelli and M. De Amici for helpful discussion. L. L. thanks the University of Pavia for partial financial support.

ABBREVIATIONS

PE, phosphatidylethanolamine; PPI, protein-protein interactions; MD, molecular dynamics; SPR, Surface Plasmon Resonance;

REFERENCES

1. World Health Organization, http://www.who.int/mediacentre/factsheets/fs094/en/. Accessed 16/05/2017
2. Ashley E, McGready R, Proux S, Nosten F (2006) Malaria. Travel Med Infect Dis 4:159-173. Doi:10.1016/j.tmaid.2005.06.009
3. Maeno Y, Culleton R, Quang NT, Kawai S, Marchand RP, Nakazawa S (2016) Plasmodium knowlesi and human malaria parasites in Khan Phu, Vietnam: Gametocyte production in humans and frequent co-infection of mosquitoes. Parasitology 144:527-535. Doi:10.1017/S0031182016002110

4. Dondorp AM, Nosten F, Yi P, Das D, Phyo AP, Tarning J, Lwin KM, Ariey F, Hanpithakpong W, Lee SJ, Ringwald P, Silamut K, Imwong M, Chotivanich K, Lim P, Herdman T, An SS, Yeung S, Singhasivanon P, Day NPJ, Lindegardh N, Socheat D, White NJ (2009) Artemisinin Resistance in Plasmodium falciparum Malaria. New Engl J Med 361:455-467. Doi:10.1056/NEJMoa0808859
5. Dondorp AM, Yeung S, White L, Nguon C, Day NPJ, Socheat D, von Seidlein L (2010) Artemisinin resistance: current status and scenarios for containment. Nat Rev Micro 8:530-530. Doi:10.1038/nrmicro2385
6. Beesley T, Gascoyne N, Knott-Hunziker V, Petursson S, Waley SG, Jaurin B, Grundström T (1983) The inhibition of class C β-lactamases by boronic acids. Biochemical J 209:229-233. Doi:10.1042/bj2090229
7. World Health Organization Malaria vaccine: WHO position paper, January 2016 – Recommendations. Vaccine. Doi:10.1016/j.vaccine.2016.10.047
8. Jana S, Paliwal J (2007) Novel molecular targets for antimalarial chemotherapy. Int J Antimicrob Ag 30:4-10. Doi:10.1016/j.ijantimicag.2007.01.002
9. Ettari R, Micale N, Grazioso G, Bova F, Schirmeister T, Grasso S, Zappalà M (2012) Synthesis and Molecular Modeling Studies of Derivatives of a Highly Potent Peptidomimetic Vinyl Ester as Falcipain-2 Inhibitors. ChemMedChem 7:1594-1600. Doi:10.1002/cmdc.201200274
10. Marco M, Coteron JM (2012) Falcipain inhibition as a promising antimalarial target. Curr Top Med Chem 12:408-444
11. Alvarez VE, Kosec G, Sant'Anna C, Turk V, Cazzulo JJ, Turk B (2008) Autophagy is involved in nutritional stress response and differentiation in Trypanosoma cruzi. J Biol Chem 283:3454-3464. Doi:10.1074/jbc.M708474200
12. Sinai AP, Roepe PD (2012) Autophagy in Apicomplexa: A life sustaining death mechanism? Trends Parasitol 28:358-364. Doi:10.1016/j.pt.2012.06.006
13. Hain AUP, Weltzer RR, Hammond H, Jayabalasingham B, Dinglasan RR, Graham DRM, Colquhoun DR, Coppens I, Bosch J (2012) Structural characterization and inhibition of the Plasmodium Atg8–Atg3 interaction. J Struct Biol 180:551-562. Doi:10.1016/j.jsb.2012.09.001
14. Besteiro S (2012) Which roles for autophagy in Toxoplasma gondii and related apicomplexan parasites? Mol Biochem Parasit 184:1-8. Doi:10.1016/j.molbiopara.2012.04.001
15. Chen D, Lin J, Liu Y, Li X, Chen G, Hua Q, Nie Q, Hu X, Tan F (2016) Identification of TgAtg8–TgAtg3 interaction in Toxoplasma gondii. Acta Trop 153:79-85. Doi:10.1016/j.actatropica.2015.09.013
16. Geng J, Klionsky DJ (2008) The Atg8 and Atg12 ubiquitin‐like conjugation systems in macroautophagy. Embo Rep 9:859
17. Abada A, Elazar Z (2014) Getting ready for building: signaling and autophagosome biogenesis. Embo Rep 15:839
18. Le Roch KG, Zhou Y, Blair PL, Grainger M, Moch JK, Haynes JD, De La Vega P, Holder AA, Batalov S, Carucci DJ, Winzeler EA (2003) Discovery of gene function by expression profiling of the malaria parasite life cycle. Science 301:1503-1508. Doi:10.1126/science.1087025
19. Duszenko M, Ginger ML, Brennand A, Gualdrón-López M, Colombo MI, Coombs GH, Coppens I, Jayabalasingham B, Langsley G, Lisboa de Castro S, Menna-Barreto R, Mottram JC, Navarro M, Rigden DJ, Romano PS, Stoka V, Turk B, Michels PAM (2011) Autophagy in protists. Autophagy 7:127-158. Doi:10.4161/auto.7.2.13310
20. Hain AU, Miller AS, Levitskaya J, Bosch J (2016) Virtual Screening and Experimental Validation Identify Novel Inhibitors of the Plasmodium falciparum Atg8-Atg3 Protein-Protein Interaction. ChemMedChem 11:900-910. Doi:10.1002/cmdc.201500515
21. Hain AUP, Bartee D, Sanders NG, Miller AS, Sullivan DJ, Levitskaya J, Meyers CF, Bosch J (2014) Identification of an Atg8-Atg3 Protein–Protein Interaction Inhibitor from the Medicines

for Malaria Venture Malaria Box Active in Blood and Liver Stage Plasmodium falciparum Parasites. J Med Chem 57:4521-4531. Doi:10.1021/jm401675a
22. Scott DE, Bayly AR, Abell C, Skidmore J (2016) Small molecules, big targets: drug discovery faces the protein-protein interaction challenge. Nat Rev Drug Discov 15:533-550. Doi:10.1038/nrd.2016.29
23. Valverde IE, Mindt TL (2013) 1,2,3-Triazoles as amide-bond surrogates in peptidomimetics. Chimia 67:262-266
24. Stucchi M, Grazioso G, Lammi C, Manara S, Zanoni C, Arnoldi A, Lesma G, Silvani A (2016) Disrupting the PCSK9/LDLR protein-protein interaction by an imidazole-based minimalist peptidomimetic. Org Biomol Chem 14:9736-9740. Doi:10.1039/C6OB01642A
25. Ni Z, Giordano L, Tenaglia A (2014) Cyclobutene Formation in PtCl2-Catalyzed Cycloisomerizations of Heteroatom-Tethered 1,6-Enynes. Chem-Eur J 20:11703-11706. Doi:10.1002/chem.201403643
26. Farmer JJ, Bhattacharjee A, Chen Y, Goldberg, A. J, Ippolito JA, Kanyo ZF, Lou R, Oyelere, K A, Sherer EC, Sutcliffe JA, Wang D, Wu, Yusheng, Du Y (2005) Preparation of macrocyclic azithromycin compounds as antibacterial, anti-proliferative and anti-inflammatory agents. PCT Int. Appl., WO 2005085266 A2, 15 Sept. 2005
27. Toma L, Legnani L, Rencurosi A, Poletti L, Lay L, Russo G (2009) Modeling of synthetic phosphono and carba analogues of N-acetyl-alpha-D-mannosamine 1-phosphate, the repeating unit of the capsular polysaccharide from Neisseria meningitidis serovar A. Org Biomol Chem 7:3734-3740. Doi:10.1039/b907000a
28. Luparia M, Legnani L, Porta A, Zanoni G, Toma L, Vidari G (2009) Enantioselective synthesis and olfactory evaluation of bicyclic alpha- and gamma-ionone derivatives: the 3D arrangement of key molecular features relevant to the violet odor of ionones. J Org Chem 74:7100-7110. Doi:10.1021/jo9014936
29. Legnani L, Colombo D, Venuti A, Pastori C, Lopalco L, Toma L, Mori M, Grazioso G, Villa S (2017) Diazabicyclo analogues of maraviroc: synthesis, modeling, NMR studies and antiviral activity. MedChemComm 8:422-433. Doi:10.1039/C6MD00575F
30. Lee C, Yang W, Parr RG (1988) Development of the Colle-Salvetti correlation-energy formula into a functional of the electron density. Phys Rev B 37:785-789
31. Becke AD (1993) Density‐functional thermochemistry. III. The role of exact exchange. J Chem Phys 98:5648-5652. Doi:10.1063/1.464913
32. Wolinski K, Hinton JF, Pulay P (1990) Efficient implementation of the gauge-independent atomic orbital method for NMR chemical shift calculations. J Am Chem Soc 112:8251-8260. Doi:10.1021/ja00179a005
33. Ditchfield R (1974) Self-consistent perturbation theory of diamagnetism. Mol Phys 27:789-807. Doi:10.1080/00268977400100711
34. Case DA, Darden TA, Cheatham TEIII; Simmerling CL, Wang J, Duke RE, Luo R, Walker C, Zhang W, Merz KM, Roberts B, Hayik S, Roitberg A, Seabra G, Swails J, Goetz AW, Kolossváry I, Wong KF, Paesani F, Vanicek J, Wolf RM, Liu J, Wu X, Brozell SR, Steinbrecher T, Gohlke H, Cai Q, Ye X, Wang J, Hsieh MJ, Cui G, Roe DR, Mathews DH, Seetin MG, Salomon-Ferrer R, Sagui C, Babin V, Luchko T, Gusarov S, Kovalenko A, and Kollman PA (2012), AMBER 12, University of California, San Francisco
35. Wang J, Wolf RM, Caldwell JW, Kollman PA, Case DA (2004) Development and testing of a general amber force field. J Comp Chem 25:1157-1174. Doi:10.1002/jcc.20035
36. Jorgensen WL, Chandrasekhar J, Madura JD, Impey RW, Klein ML (1983) Comparison of simple potential functions for simulating liquid water. J Chem Phys 79:926-935. Doi:10.1063/1.445869

37. Essmann U, Perera L, Berkowitz ML, Darden T, Lee H, Pedersen LG (1995) A smooth particle mesh Ewald method. J Chem Phys 103:8577-8593
38. Berendsen HJC, Postma JPM, Gunsteren WFv, DiNola A, Haak JR (1984) Molecular dynamics with coupling to an external bath. J Chem Phys 81:3684-3690. Doi:10.1063/1.448118
39. Jones G, Willett P, Glen RC, Leach AR, Taylor R (1997) Development and validation of a genetic algorithm for flexible docking. J Mol Biol 267:727-748. Doi:10.1006/jmbi.1996.0897
40. Korb O, Stutzle T, Exner TE (2009) Empirical scoring functions for advanced protein-ligand docking with PLANTS. J Chem Inf Model 49:84-96. Doi:10.1021/ci800298z
41. Dallanoce C, Magrone P, Bazza P, Grazioso G, Rizzi L, Riganti L, Gotti C, Clementi F, Frydenvang K, De Amici M (2009) New Analogues of Epiboxidine Incorporating the 4,5-Dihydroisoxazole Nucleus: Synthesis, Binding Affinity at Neuronal Nicotinic Acetylcholine Receptors, and Molecular Modeling Investigations. Chem Biodivers 6:244-259. Doi:10.1002/cbdv.200800077
42. Nilsson BM, Vargas HM, Ringdahl B, Hacksell U (1992) Phenyl-substituted analogues of oxotremorine as muscarinic antagonists. J Med Chem 35:285-294
43. Frisch MJ, Trucks GW, Schlegel HB, Scuseria GE, Robb M, A, Cheeseman JR, Scalmani G, Barone V, Mennucci B, Petersson GA, Nakatsuji H, Caricato M, Li X, Hratchian HP, Izmaylov AF, Bloino J, Zheng G, Sonnenberg JL, Hada M, Ehara M, Toyota K, Fukuda R, Hasegawa J, Ishida M, Nakajima T, Honda Y, Kitao O, Nakai H, Vreven T, Montgomery JJ, A., Peralta JE, Ogliaro F, Bearpark M, Heyd JJ, Brothers E, Kudin KN, Staroverov VN, Kobayashi R, Normand J, Raghavachari K, Rendell A, Burant JC, Iyengar SS, Tomasi J, Cossi M, Rega N, Millam JM, Klene M, Knox JE, Cross, B. J, Bakken V, Adamo C, Jaramillo J, Gomperts R, Stratmann, ER, Yazyev O, Austin AJ, Cammi R, Pomelli C, Ochterski WJ, Martin RL, Morokuma K, Zakrzewski VG, Voth GA, Salvador P, Dannenberg JJ, Dapprich S, Daniels AD, Farkas Ö, Foresman JB, Ortiz JV, Cioslowski J, Fox DJ (2009) Gaussian09. Revision A.02.
44. Trager W, Jensen JB (1976) Human malaria parasites in continuous culture. Science 193:673-675